



UNIVERSITY OF LEEDS

This is a repository copy of *Influence of growth kinetics on Sn incorporation in direct band gap Ge<sub>1-x</sub>Sn<sub>x</sub> nanowires*.

White Rose Research Online URL for this paper:  
<http://eprints.whiterose.ac.uk/139820/>

Version: Accepted Version

---

**Article:**

Doherty, J, Biswas, S, Saladukha, D et al. (5 more authors) (2018) Influence of growth kinetics on Sn incorporation in direct band gap Ge<sub>1-x</sub>Sn<sub>x</sub> nanowires. *Journal of Materials Chemistry C*, 6 (32). pp. 8738-8750. ISSN 2050-7526

<https://doi.org/10.1039/c8tc02423e>

---

This journal is © The Royal Society of Chemistry 2018. This is an author produced version of a paper published in *Journal of Materials Chemistry C*. Uploaded in accordance with the publisher's self-archiving policy.

**Reuse**

Items deposited in White Rose Research Online are protected by copyright, with all rights reserved unless indicated otherwise. They may be downloaded and/or printed for private study, or other acts as permitted by national copyright laws. The publisher or other rights holders may allow further reproduction and re-use of the full text version. This is indicated by the licence information on the White Rose Research Online record for the item.

**Takedown**

If you consider content in White Rose Research Online to be in breach of UK law, please notify us by emailing [eprints@whiterose.ac.uk](mailto:eprints@whiterose.ac.uk) including the URL of the record and the reason for the withdrawal request.



[eprints@whiterose.ac.uk](mailto:eprints@whiterose.ac.uk)  
<https://eprints.whiterose.ac.uk/>

# Influence of Growth Kinetics on Sn Incorporation in Direct Band gap $\text{Ge}_{1-x}\text{Sn}_x$ Nanowires

Jessica Doherty<sup>1,2,3</sup>, Subhajit Biswas<sup>1,2,3\*</sup>, Dzianis Saladukha<sup>3</sup>, Quentin Ramasse<sup>4</sup>, Tara Shankar Bhattacharya<sup>5</sup>, Achintya Singha<sup>5</sup>, Tomasz J. Ochalski<sup>3</sup>, and Justin D. Holmes<sup>1,2,3</sup>

<sup>1</sup>School of Chemistry, University College Cork, Cork, Ireland. <sup>2</sup>Tyndall National Institute, University College Cork, Cork, Ireland. <sup>3</sup>AMBER@CRANN, Trinity College Dublin, Dublin 2, Ireland.

<sup>4</sup>SuperSTEM Laboratory, SciTech Daresbury Campus, Daresbury WA4 4AD, United Kingdom.

<sup>5</sup>Department of Physics, Bose Institute, Kolkata, India.

## Corresponding Author

Tel: +353 (0)21 490 5143; E-mail: s.biswas@ucc.ie

## Abstract

$\text{Ge}_{1-x}\text{Sn}_x$  alloys with substantial incorporation of Sn show promise as direct bandgap group IV semiconductors. This article reports the influence of growth kinetics on Sn inclusion in  $\text{Ge}_{1-x}\text{Sn}_x$  alloy nanowires through manipulation of the growth constraints, i.e. temperature, precursor type and catalyst.  $\text{Ge}_{1-x}\text{Sn}_x$  nanowire growth kinetics were manipulated in a vapour-liquid-solid (VLS) growth process by varying the growth temperature between 425 and 470 °C, using Au and Ag alloy as growth catalysts and different tin precursors such as allyltributyltin, tertaethyltin and tetraallyltin. The profound impact of growth kinetics on the incorporation of Sn; from 7 to 9 at. %; in  $\text{Ge}_{1-x}\text{Sn}_x$  nanowires was clearly apparent, with the fastest growing nanowires (of comparable diameter) containing a higher amount of Sn. A kinetically dependent “solute trapping” process was assigned as the primary inclusion mechanism for Sn incorporation in the  $\text{Ge}_{1-x}\text{Sn}_x$  nanowires. The participation of a kinetic dependent, continuous Sn incorporation process in the single-step VLS nanowire growth resulted in improved ordering of the  $\text{Ge}_{1-x}\text{Sn}_x$  alloy lattice; as opposed to a randomly ordered alloy. The amount of Sn inclusion and the Sn impurity ordering in  $\text{Ge}_{1-x}\text{Sn}_x$  nanowires has a profound effect on the quality of the light emission and on the directness of the band gap as confirmed by temperature dependent photoluminescence study and electron energy loss spectroscopy.

## Introduction

A major hindrance to the integration of group IV materials in optoelectronic devices is the lack of a direct bandgap in both Si and Ge.<sup>1</sup> A direct bandgap group IV semiconductor would be beneficial for efficient band-to-band tunnelling devices, such as a tunnelling field effect transistor (TFET),<sup>2,3</sup> for lasing platforms<sup>4,5</sup> and for the development of mid-IR photonic devices such as waveguide amplifiers and multi-wavelength light sources.<sup>6</sup> A number of researchers have reported both theoretically and experimentally that a direct bandgap can be achieved in Ge by alloying the semiconductor with Sn,<sup>7,8</sup> lowering the separation between indirect (L) and direct ( $\Gamma$ ) valleys (140 meV in bulk Ge) in the conduction band of Ge.<sup>9</sup>

The fabrication of direct bandgap  $\text{Ge}_{1-x}\text{Sn}_x$  alloys in 1D nanoforms is imperative for the manufacturing of nanoelectronic devices, such as TFETs and gate-all-around FETs<sup>2,3,10</sup> as the 1D morphology provides excellent electrostatic control over the channel. Unlike Si and SiGe nanosystems, where an external perturbation such as strain is necessary to obtain a direct bandgap transition,<sup>10</sup> a direct bandgap transition in  $\text{Ge}_{1-x}\text{Sn}_x$  nanowires can be obtained through band mixing and deformation.<sup>11,12</sup> The generation of  $\text{Ge}_{1-x}\text{Sn}_x$  nanowires have been previously reported via both top-down fabrication<sup>13,14</sup> and bottom-up growth.<sup>15–17</sup> However, the etch chemistry required to fabricate highly crystalline, uniform top-down  $\text{Ge}_{1-x}\text{Sn}_x$  nanowires is, as of yet, still in its infancy, and bottom-up grown nanowires often exhibit low aspect ratios and non-uniform morphologies, with bending and kinking, thus restricting efficient light emission from these materials.<sup>15</sup> Taking account of the lack of optically efficient group IV alloy nanomaterials, we have recently reported the fabrication of direct bandgap  $\text{Ge}_{1-x}\text{Sn}_x$  nanowires with up to 9.2 at. % Sn via a two-step catalytic bottom up growth.<sup>12</sup> In this approach, Sn was incorporated into the Ge nanowire at the growth temperature during VLS growth<sup>18,19</sup> and an additional after-growth dissolution process at the Ge-Sn eutectic temperature, resulting high incorporation of Sn in Ge where Sn atoms are randomly ordered in the  $\text{Ge}_{1-x}\text{Sn}_x$  lattice. Impurity ordering in semiconductor alloys provide an additional engineering of

freedom as the ordering is associated with the electronic band structure such as reduction of band gap, degeneracy at the valence band, emission width and lifetime.<sup>20,21</sup> In case of Ge<sub>1-x</sub>Sn<sub>x</sub> nanowire, a randomly ordered alloy resulted in luminescence with broad line-widths which are not ideal for photonic devices.<sup>12</sup>

Therefore, incorporation of a substantial amount ( $x > 0.09$  is desired for direct band gap) of Sn into a 1D Ge host lattice during VLS growth process, where the impurity atoms are assimilated directly and in a more ordered way during the three phase growth via solute-trapping, is imperative for further engineering of the band structure and emission characteristics of Ge<sub>1-x</sub>Sn<sub>x</sub> nanowires. A perfectly binary/ternary alloy would produce a completely random distribution in terms of atomic ordering of impurities. A deviation from this random distribution can generate “short-range ordering”<sup>20</sup> of at least one of the atomic constituents of the alloy with an impact on the basic properties of the alloyed semiconductors.<sup>22,23</sup> The uniform and relatively ordered distribution of Sn impurities in a 1-D alloy lattice during the VLS nanowire growth can be achieved via the “solute trapping” process, where the impurities are incorporated by solute redistribution at the catalyst-nanowire interface via an increase of chemical potential and deviation of the partition coefficient.<sup>12,18,19,24</sup> As a kinetic dependent incorporation model, solute trapping of foreign adatoms, *i.e.* the incorporation of Sn impurities, can be altered/controlled by influencing the kinetics of the growth system. Manipulation of the rate determining steps in VLS growth allows the velocity at which nanowires grow to be controlled thus giving an opportunity to engineer impurity incorporation. Growth kinetics of semiconductor nanowires can be modified by influencing the concentration of the growth species in the vapour phase, by using high temperatures to induce faster cracking of precursors or by using precursors with higher catalytic decomposition rates. These growth parameters directly influence supersaturation;  $\Delta\mu$ ; to manipulate the growth rate of nanowires by altering the partial pressure of the vapour source. Increased supersaturation and hence the nanowire growth rate can also be achieved by lowering the equilibrium concentration ( $C_e$ ) of the growth species in the liquid seeds in the VLS growth, with the use of bi-metallic growth catalysts.<sup>24</sup>

This article describes how growth parameters such as temperature, precursor and catalyst composition influence  $\text{Ge}_{1-x}\text{Sn}_x$  nanowire growth kinetics. We demonstrate the influence of nanowire growth kinetics on the subsequent solute trapping and incorporation of Sn in the  $\text{Ge}_{1-x}\text{Sn}_x$  nanowires. The quantitative (amount of Sn) and qualitative (homogeneity and ordering of Sn) characteristics of Sn incorporation in  $\text{Ge}_{1-x}\text{Sn}_x$  is verified through elemental microscopic analysis, high resolution microscopy and Raman spectroscopy. Influence of Sn concentration and ordering on the nature of the light emission (band gap transition, emission widths, band gap *etc.*) from the  $\text{Ge}_{1-x}\text{Sn}_x$  alloy nanowires are also explored via temperature dependent photoluminescence and electron energy loss spectroscopy.

## Experimental

For the growth of  $\text{Ge}_{1-x}\text{Sn}_x$  nanowires dodecanethiol-stabilised, phase pure, Au and AuAg alloy nanoparticles were used as growth seeds. Colloidal nanoparticles were synthesised by co-reducing a mixture of chloroauric acid ( $\text{HAuCl}_4$ ) and silver nitrate ( $\text{AgNO}_3$ ) in a chloroform/water biphasic solution.<sup>12,25–27</sup> These metal nanoparticles were spin-coated onto a Si (001) substrate with native oxide. The substrate was loaded into a metal reaction vessel which was then left under vacuum at 180 °C overnight to ensure a moisture free growth atmosphere and the desorption of the surfactant molecules.

Solutions of diphenylgermane (DPG) and Sn precursors in anhydrous toluene were prepared in an  $\text{N}_2$  filled glove box with a typical Ge and Sn precursor concentration of 0.025 mL and 0.0075 mL respectively in 10 mL toluene. A solution containing both Ge and Sn precursors was loaded into a Hamilton sample-lock syringe inside the nitrogen-filled glovebox. Prior to injection, the coated Si substrate was further annealed for 15 min at 440 °C under a flowing  $\text{H}_2/\text{Ar}$  atmosphere inside a tube furnace. The precursor solution was then injected into the metal reaction vessel using a high-pressure syringe pump at a rate of

0.025 mL min<sup>-1</sup>. A H<sub>2</sub>/Ar flow rate of 0.6 sccm was maintained during the entire growth period. A typical nanowire growth time was 2 h.

To explore the limits of kinetic dependent solute trapping of Sn impurities in Ge nanowires, the following parameters of the system were varied; temperature, catalyst and precursor. The growth temperature was varied in 15 °C increments from 425 °C to 470 °C. Three different precursors, allyltributylstannane (ATBS), tetraallyltin (TAT) and tetraethyltin (TET), were used as the Sn source. Also, phase pure Au and AuAg alloy nanoparticles (Au<sub>0.90</sub>Ag<sub>0.10</sub> and Au<sub>0.80</sub>Ag<sub>0.20</sub> nanoparticles) of 4-5 nm diameter were explored as catalysts (see Supporting Info Figure S1).

## Characterisation

Bottom-up grown Ge<sub>1-x</sub>Sn<sub>x</sub> nanowires were imaged on a FEI Helios NanoLab 600i scanning electron microscope (SEM). All energy-dispersive X-ray (EDX) measurements were recorded in high-angle annular dark-field mode in the FEI Helios NanoLab 600i operating at 30 kV and 0.69 nA with an attached Oxford X-Max 80 detector. Error in the EDX measurements indicates a standard error of 0.5 at. %. Nanowire length and diameter measurements were determined using SEM images on ImageJ, in which the nanowires were clearly visible from end to end. Mean values for the length and diameter of the nanowires were determined from a minimum of 50 nanowires. Helium Ion Microscope (HIM) images were obtained using a Zeiss ORION Nanofab. TEM analysis was performed on a JEOL JEM-2100 operating at 200 kV in bright-field condition for imaging. High-resolution STEM imaging and EELS mapping was performed using a Nion UltraSTEM100 microscope, operated at 100 kV. Probe-forming optics were adjusted to deliver a 0.9 Å probe, with 120 pA beam current and 31 mrad convergence semi-angle. EELS data were acquired on a Gatan Enfina spectrometer, at 1 eV per channel to capture both the Sn and Ge edges simultaneously. As a result, the effective energy resolution was limited to 2.5 eV by the detector point spread function (B3 pixels), even though the cold field emission gun of the instrument had

a native energy width of 0.35 eV in the operating conditions. Raman scattering measurements were performed in a backscattering geometry using a micro-Raman setup consisting of a spectrometer (model LabRAM HR, Jobin Yvon) and a Peltier-cooled charge-coupled device detector. An air cooled He-Ne laser of wavelength 488 nm with intensity of  $1.77 \times 10^7 \text{ W/m}^2$  was used as an excitation source. PL data was obtained using a Ti:Sa pulsed laser as the excitation source, tuned to 950 nm with 80 MHz repetition rate, 300 fs pulse width and 0.2 W average power. The laser spot was focused to a 9  $\mu\text{m}$  spot, providing 200  $\text{kW/cm}^2$  of pump power density. Samples were chilled in liquid nitrogen cryostat down to 80 K. PL was detected by a liquid nitrogen chilled InAs detector with a sensitivity range from 0.9  $\mu\text{m}$  to 3  $\mu\text{m}$  ( $\sim 0.41$ - $1.338$  eV). Thermogravimetric Analysis (TGA) was carried out on a Mettler Toledo TGA/DSC 1 Star System using a 20  $^\circ\text{C}/\text{min}$  ramp rate from 25 to 600  $^\circ\text{C}$  under a flow of nitrogen gas.

## Results and Discussion

The growth kinetics of the  $\text{Ge}_{1-x}\text{Sn}_x$  nanowires can be influenced through the manipulation of the growth parameters of the system. Increased growth kinetics should result in a faster growth rate, and therefore longer nanowires. Solute trapping, a kinetically dependent trapping model,<sup>18,19</sup> directly links nanowire growth rate to impurity incorporation. Any impurity, such as Sn, incorporation through solute trapping should increase with increasing nanowire growth kinetics. Therefore, controlling the  $\text{Ge}_{1-x}\text{Sn}_x$  nanowire growth parameters should allow optimisation of Sn incorporation into the nanostructures. The growth kinetics of nanowires fabricated via VLS growth are dependent on the following: (i) the incorporation of the growth species from the vapour phase to the liquid growth promoter, (ii) the diffusion of the growth species inside the liquid melt and (iii) crystallisation of the growth material at the liquid-solid interface.<sup>28</sup> In a supersaturation limited process, the rate determining steps for VLS growth are believed to be steps (i)<sup>29,30</sup> and (iii).<sup>28</sup> The supersaturation,  $\Delta\mu$ , is the chemical potential difference between adatoms of the growth species in the vapour phase and the solid crystal phase<sup>26</sup> with  $v \propto \left[ \frac{\Delta\mu}{kT} \right]^2$ , where  $v$  is the growth velocity of a crystal. Supersaturation directly influences nanowire growth kinetics and can be manipulated



via the use of catalysts with different equilibrium concentration of growth species<sup>31</sup> (Supporting Info, Equation S1). Incorporation of the growth species into the liquid seed can also be manipulated to promote faster growth kinetics by employing higher temperatures<sup>32</sup> and precursors with high catalytic decomposition rates.

To understand the influence temperature had on the growth kinetics and on Sn incorporation in the nanowires, and to determine the optimum growth temperature, the temperature was varied from 425 to 470 °C in increments of 15 °C. Growth kinetics have previously been shown to heavily influence the Sn incorporation in GeSn films<sup>33,34</sup> where the Sn incorporation decreases with increasing temperature, while growth rate increases. However as of yet there has been no such verification on the influences of temperature on Sn incorporation in GeSn nanowires. We have limited the temperature range deliberately between 425 and 470 °C as; (i) below 425 °C the nanowire yield becomes poor due to poor decomposition of Ge precursor (DPG) and (ii) above 470 °C due to fast decomposition of low boiling point Sn precursors, homogenous nucleation of Sn dominates resulting in spherical Sn clusters and a possible decrease in Sn content in the nanowires. The other experimental parameters ( $\text{Au}_{0.90}\text{Ag}_{0.10}$  nanoparticle catalyst and Ge:Sn initial molar ratio of 85:15) were kept constant, based on prior  $\text{Ge}_{1-x}\text{Sn}_x$  nanowire growth experience<sup>12</sup> using DPG and ATBS as Ge and Sn precursors respectively. Figure 1 shows SEM images of  $\text{Ge}_{1-x}\text{Sn}_x$  nanowires grown at temperatures ranging from 425 to 455 °C. Distribution of nanowire lengths for each temperature is depicted in Figure 1(d) and shows the growth of the longest nanowires at 440 °C. The mean Sn content in the nanowires grown at different temperature is provided in Figure 1(e). The nanowires grown at 440 °C, with a mean length of  $2.21 \pm 1.35 \mu\text{m}$ , contained the highest Sn content (6.5 at. %). Also, the formation of spherical Sn clusters was minimal for nanowires grown at 440 °C, as shown in Figure 1(b).

High growth temperatures can influence the precursor decomposition and partial precursor pressure and hence the incorporation of growth species into the catalyst during VLS growth, thus increasing the nanowire growth velocity. Also, in contrary, considering the nanowire growth as a crystallisation limited process, longer nanowires at lower growth temperatures could be justified from classical crystal growth theory,<sup>26,28</sup> as growth velocity ( $v$ ) is proportional to  $\left(\frac{\Delta\mu}{kT}\right)^2$ , where  $T$  is the synthesis temperature and  $\Delta\mu$  is supersaturation. However, in our atmospheric pressure VLS experiments the effect of temperature on the growth kinetics is influenced by both the kinetic driven precursor decomposition at elevated temperature and crystallisation at the triple-phase interface. The change in the growth temperature was minimal (between 425 to 470 °C) to negate heavily influencing the decomposition of DPG and ATBS to affect the partial precursor pressure and incorporation of Ge and Sn in the catalysts, with both catalysts decomposing below 425 °C. Whereas the crystallisation at the triple phase interface at different temperatures can play a defining role in determining the overall rate of nanowire growth and thus the extent of Sn incorporation. Competitive kinetics between these two temperature dependent processes determine the nanowire growth kinetics. At high growth temperatures (455 and 470 °C), the lower Sn content in the nanowires compared to the nanowires grown at 440 °C (Figure 1(e)) could be a direct result of the slower growth kinetics (mean nanowire length of 2.21  $\mu\text{m}$  at 440 °C compared to 1.55  $\mu\text{m}$  at 455 °C) resulted from slow crystallisation at triple phase boundary at elevated temperature.

To further investigate suitable Sn impurity precursors for improving Sn incorporation in the  $\text{Ge}_{1-x}\text{Sn}_x$  nanowires, alternative Sn sources to ATBS were utilised, *i.e.* tetraallyltin (TAT, boiling point of 269 °C) and tetraethyltin (TET, boiling point of 181 °C). Precursors whose boiling points were much lower than ATBS (353 °C) were chosen in an effort to promote faster decomposition and higher Sn incorporation. The optimal growth temperature was held at 440 °C with other precursors, as higher growth temperature would result in rather fast precursor decomposition and homogenous Sn nucleation. In each of these compounds, the Sn molecule is bonded to four carbon atoms by single bonds. ATBS, as previously shown

in Figure 1, is a suitable precursor for incorporating large amounts (6.5 at. %) of Sn into the Ge lattice while keeping the structural and morphological quality intact. High Sn incorporation and controlled nanowire morphology with ATBS as a Sn precursor is due to the similar decomposition kinetics and boiling points of ATBS and diphenyl germane (DPG), 353 and 325 °C respectively at atmospheric pressure. Using TAT as a Sn source resulted in  $\text{Ge}_{1-x}\text{Sn}_x$  nanowires with an overall lower Sn content of < 2 at. % with an  $\text{Au}_{0.90}\text{Ag}_{0.10}$  catalyst (Supporting Info, Figure S2). Significant Sn segregation and spherical clustering was apparent when TAT was used as the Sn source (Supporting Info, Figure S2), compared with ATBS or TET. This clustering, and low Sn incorporation, may be due to the instability of TAT under the reaction conditions due to the presence of four carbon-carbon double bonds<sup>35</sup>. Thermogravimetric analysis (TGA) of the Sn precursors revealed that their decomposition temperatures related directly to their boiling points (Supporting Info, Figure S3).

The third Sn precursor of choice, TET, produced long  $\text{Ge}_{1-x}\text{Sn}_x$  nanowires with a high Sn content, negligible Sn clustering and uniform diameter ( $57.4 \pm 15.2$  nm) with the  $\text{Au}_{0.90}\text{Ag}_{0.10}$  nanoparticle catalyst (Figure 2). An initial Ge:Sn molar ratio of 77:23 was determined as optimal for the growth of  $\text{Ge}_{1-x}\text{Sn}_x$  nanowires; a Ge:Sn molar ratio of 85:15, which was used with ATBS as the Sn source, resulted in ‘branched’ nanowires consisting of a large nanowire “trunk” with smaller nanowire “branches” (Supporting Info, Figure S4). An SEM image of the nanowires grown at 440 °C using TET with an  $\text{Au}_{0.90}\text{Ag}_{0.10}$  catalyst is shown in Figure 2(a). A mean Sn concentration of  $8.7 \% \pm 0.7 \%$  was determined via EDX analysis of the nanowires grown with TET as a precursor, an increase of 2.2 at. % when compared to nanowires grown under the same conditions using ATBS (6.5 at. % Sn). To ensure that the Sn in these  $\text{Ge}_{1-x}\text{Sn}_x$  nanowires was homogeneously distributed in the nanowire, *i.e.* without Sn segregation in the bulk or surface of the nanowire or a gradual decrease in the Sn content from the seed to the end of a nanowire, EDX maps (Figure 2(b)) and linescans (Supporting Info, Figure S5) were obtained for individual nanowires. The lack of Sn segregation is verified by the absence of bright red spots

(corresponding to Sn) in the elemental map shown in Figure 2(b). Precursor choice had a clear impact on the Sn incorporation of the  $\text{Ge}_{1-x}\text{Sn}_x$  nanowires, with TET producing nanowires with the highest Sn content while maintaining uniform diameter and negligible tapering. As encouraging results in terms of morphology and Sn content was obtained with TET at 440 °C, an experiment was carried out at 470 °C using TET as the Sn source to verify the influence of temperature with TET as Sn precursor. This elevated temperature resulted in a lower yield of nanowires, numerous spherical Sn clusters and erratic Sn content (between 4 – 8 at.%) in the nanowires (Supporting Information, Figure S6). Though decreasing the temperature may have positive influence on triple phase crystallisation (independent of precursor characteristics) we did not observe increase in growth rate at 425 °C with ATBS. Thus we have restricted experiments with TET between 440 and 470 °C.

An alternative method to increase the growth rate and thus potentially the Sn incorporation in  $\text{Ge}_{1-x}\text{Sn}_x$  nanowires is to increase the supersaturation  $\Delta\mu$ ; chemical potential difference between adatoms of growth species in the vapor phase and the solid crystal phase; as per classical crystal growth theory.<sup>28</sup> A higher  $\Delta\mu$  promotes a faster crystallisation rate, thus increasing the growth velocity of the nanowire. In our previous work, we demonstrated an effective way to increase the supersaturation for the group IV nanowires by lowering the equilibrium concentration ( $C_e$ ) of the growth material in a liquid metastable alloy, *e.g.* Au-Ge, as  $\Delta\mu = kT \ln\left(\frac{C}{C_e}\right)$  where C is the concentration of the growth species. To lower the  $C_e$  of a growth species, a foreign species can be added to the metal seed particle which will shift the liquidus phase boundary of the growth species towards a lower solute concentration. For a nanoscopic system having high surface-to-volume ratio, the contribution of the surface energy to the thermodynamics is prominent, resulting in a diameter dependent growth rate. Nanowire growth and the expression ( $\Delta\mu = \Delta\mu_0 - \frac{4\Omega\alpha}{d}$ ) for radial dependent chemical potential and hence supersaturation clearly indicate a growth rate increment with a decrease in equilibrium concentration of Ge in the metastable phase, as  $\Delta\mu \propto$

$\ln\left(\frac{c}{c_e}\right)$  for a certain diameter range. For Ge nanowires, alloying Au catalyst seeds with Ag (up to a certain limit of Au<sub>0.80</sub>Ag<sub>0.20</sub>) promotes growth rates of up to 5 times as fast when compared to the growth with pure Au.<sup>26</sup> AuAg metal alloy catalysts trigger faster growth rates for the same diameter ( $d$ ) nanowires when compared to those grown from a pure Au catalyst, due to the change in equilibrium concentration of Ge and thus supersaturation in the metastable liquid alloy. Taking account of this influence of alloy seeds on the nanowire growth, phase pure Au and three AuAg alloy nanoparticles (Au<sub>0.90</sub>Ag<sub>0.10</sub>, Au<sub>0.80</sub>Ag<sub>0.20</sub> and Au<sub>0.70</sub>Ag<sub>0.30</sub>) were explored as catalysts for Ge<sub>1-x</sub>Sn<sub>x</sub> growth. All of the nanoparticle catalysts had diameters between 4-5 nm (Supporting Info, Figure S1). TET, which was determined as an ideal Sn precursor for large Sn incorporation, was used as the precursor with all three catalysts. An increase in the length, as well as Sn content, of the nanowires was observed in correspondence with increasing Ag in the nanoparticle alloys (Figure 3). Au seeded nanowires grown at 440 °C with TET as a tin source contained 7.4 at. % Sn, whereas those seeded with Au<sub>0.90</sub>Ag<sub>0.10</sub> and Au<sub>0.80</sub>Ag<sub>0.20</sub> seed under the same growth conditions contained 8.7 at. % and 9.1 at. % respectively. With a further increase in the amount of Ag in the AuAg seed, the nanowires catalysed by Au<sub>0.70</sub>Ag<sub>0.30</sub> contained large amounts of Sn (~10.9 at. % Sn) however the resulting nanowires were low in yield, had irregular morphologies and were highly tapered (Supporting Info, Figure S7). The tin distribution in Au<sub>0.70</sub>Ag<sub>0.30</sub> catalysed Ge<sub>1-x</sub>Sn<sub>x</sub> nanowires was also not uniform as depicted by EDX analysis (see EDX linescan in Supporting Info, Figure S7(b)). As such, Au<sub>0.80</sub>Ag<sub>0.20</sub> nanoparticles were found to be the optimal catalyst for Ge<sub>1-x</sub>Sn<sub>x</sub> nanowire growth with TET as the Sn precursor, giving a high Sn content, uniform diameter nanowires (~60 nm), with no apparent evidence of nanowire tapering. An SEM image of Ge<sub>1-x</sub>Sn<sub>x</sub> nanowires grown with an Au<sub>0.80</sub>Ag<sub>0.20</sub> catalyst and TET as the precursor at 440 °C can be seen in Figure 3(a). EDX point analysis on 50 nanowires provided an average Sn content of  $9.1 \pm 1.3$  at. % Sn in these Ge<sub>1-x</sub>Sn<sub>x</sub> nanowires. EDX maps and linescans were generated to confirm the homogenous distribution of Sn in the nanowires (Supporting Info, Figure S8). The lack of bright red spots in the body of the nanowires in the elemental map (Supporting Info, Figure S8(b)) further suggests the lack of Sn clustering and segregation in the bulk

or on the surface of the nanowires. Figure 3(c) summarises the variation in the amount of Sn in the  $\text{Ge}_{1-x}\text{Sn}_x$  nanowires with increasing Ag in the nanoparticle catalyst. To verify the increased growth rate of these  $\text{Ge}_{1-x}\text{Sn}_x$  nanowires with increasing Ag content in the nanoparticle, the lengths of these nanowires were compared for similar diameters across the samples. As the nanowires catalysed by  $\text{Au}_{0.70}\text{Ag}_{0.30}$  were irregular in both diameter and length and highly tapered, they were not included in the length comparison. The mean diameter of the nanowires catalysed with Au,  $\text{Au}_{0.90}\text{Ag}_{0.10}$  and  $\text{Au}_{0.80}\text{Ag}_{0.20}$  were in a similar size range;  $63.5 \pm 17.4$  nm,  $57.4 \pm 15.2$  nm and  $65.5 \pm 16.8$  nm respectively. This similarity in diameter excludes the influence of diameter on the growth kinetics (Gibbs-Thompson effect) which allows a direct comparison between the mean lengths of the  $\text{Ge}_{1-x}\text{Sn}_x$  nanowires grown from different seeds. The histogram shown in Figure 3(d) depicts the increasing mean nanowire length ( $2.44 \pm 1.54$   $\mu\text{m}$ ,  $2.63 \pm 1.63$   $\mu\text{m}$  and  $3.6 \pm 1.51$   $\mu\text{m}$  with Au,  $\text{Au}_{0.90}\text{Ag}_{0.10}$  and  $\text{Au}_{0.80}\text{Ag}_{0.20}$  catalysts respectively) with increasing Ag content in the nanoparticle catalyst. Thus the growth kinetics of  $\text{Ge}_{1-x}\text{Sn}_x$  nanowires have been increased by increasing the Ag content of the  $\text{Au}_x\text{Ag}_{1-x}$  catalysts. This increase in the growth kinetics manifests itself in increased Sn incorporation in the Ge nanowires with the  $\text{Au}_{0.80}\text{Ag}_{0.20}$  growth promoter (Figure 3(c)). During the nanowire growth process, with uptake of Sn from the vapour phase, the nanoparticle catalyst becomes largely Sn rich (Supporting Info, Figure S8). However, the initial composition of the AuAg nanoparticle catalyst influences the supersaturation of the system, which in turn impacts the nucleation and growth rate,<sup>36</sup> which is apparent from Figure 3(d).

Through the manipulation of the growth limiting factors of the  $\text{Ge}_{1-x}\text{Sn}_x$  nanowire system the growth kinetics have been influenced. This influence manifests itself in the increased growth rates and thus increased lengths of the nanowires. A distribution of the lengths of  $\text{Ge}_{1-x}\text{Sn}_x$  nanowires with 6.5, 7.4, 8.7 and 9.1 at. % Sn (Supporting Info, Figure S9(a)) details the relationship between the length and the Sn content. By influencing the growth kinetics to increase the growth rate of the  $\text{Ge}_{1-x}\text{Sn}_x$  nanowires, the Sn incorporation of the nanowires has been positively impacted. A comparison of the mean Sn content

relative to the mean nanowire length of the  $\text{Ge}_{1-x}\text{Sn}_x$  nanowires (Supporting Info, Figure S9(b)) confirms the correlation between the growth kinetics of the system and the incorporation of Sn impurities. The increased growth kinetics of the  $\text{Ge}_{1-x}\text{Sn}_x$  nanowires, obtained by manipulating the growth limiting factors of the system, has resulted in nanowires with 9.1 at. % Sn through conventional VLS growth.

In the case of  $\text{Ge}_{1-x}\text{Sn}_x$  nanowires, due to the dependence of the Sn incorporation on the nanowire growth kinetics, we assert that Sn is incorporated via the solute trapping mechanism, a kinetically driven process,<sup>12,37</sup> as indicated by the increasing Sn inclusion with increasing length (Figure 3(d)). In the case of nanowires, solute trapping has already been suggested as the method of incorporation of Al, from the catalyst, into Si nanowires<sup>24</sup> where increased temperature resulted in faster growth kinetics of nanowire and higher Sn incorporation. Assuming layer by layer growth of the nanowires,<sup>38,39</sup> the step flow kinetics can result in solute trapping of Sn by each succeeding layer of the nanowire. Solute trapping describes the incorporation of impurities by solute redistribution at the catalyst-nanowire interface; there is an increase of chemical potential and deviation of the partition coefficient.<sup>18,19,40</sup> At this liquid-solid (catalyst-nanowire) interface, the difference in atomic concentration in the different phases is characterised by the equilibrium coefficient of the atomic distribution between phases,  $k_e$ . This equilibrium partition coefficient is related to the chemical potential difference, *i.e.* supersaturation  $\Delta\mu$ ; by  $k_e \propto \exp\left(-\frac{\Delta\mu}{RT}\right)$ . During nanowire growth, the large interface velocity at the liquid-solid interface relaxes the local chemical equilibrium which results in kinetic interface undercooling.<sup>41</sup> Impurity adatoms can be trapped on the high energy sites of the crystal lattice at a high solidification rate which can lead to the formation of metastable solids ( $\text{Ge}_{1-x}\text{Sn}_x$  with  $x > 0.01$ ) at the growth front.<sup>12</sup> This deviation of the chemical equilibrium at the interface is influenced by the interfacial diffusion speed,  $V_{DI}$ , a kinetic parameter where  $V_{DI} = -\frac{D_I}{\lambda}$ .  $V_{DI}$  is a ratio of the diffusion coefficient at the interface ( $D_I$ ) and the characteristic distance for the diffusion jump ( $\lambda$ ) which is equal to the width of the solid-liquid interface.<sup>18</sup>

For a given system with an equilibrium partition coefficient  $k_e$  and an interfacial diffusion  $V_{DI}$ , the amount of impurity trapped in the nanowire is governed by equation 1<sup>18</sup>:

$$k(V) = \frac{\left(1 - V^2/V_D^2\right) k_e + \frac{V}{V_{DI}}}{1 - V^2/V_D^2 + \frac{V}{V_{DI}}} \dots (Eq. 1)$$

Hence, as  $V$ , the interface velocity approaches infinity,  $k(V)$ , the solute partitioning function, approaches 1. Therefore, when the interfacial velocity is much greater than the diffusion speed ( $V_D$ , the characteristic bulk speed) solute trapping will increase with complete solute trapping at  $k(V) = 1, V \geq V_D$ . As such, impurity incorporation is primarily dependent on the interfacial velocity. In the case of  $\text{Ge}_{1-x}\text{Sn}_x$  nanowire, very slow bulk diffusion velocity of Sn in  $\text{Ge}^{42}$  allows for the solute trapping of Sn to occur at the relatively slow interfacial growth velocity of the  $\text{Ge}_{1-x}\text{Sn}_x$  nanowires.

Hence, a variation in the interfacial velocity and nanowire growth kinetics during bottom-up VLS growth will influence the solute partitioning function and thus the “solute trapping” of an impurity into a nanowire. Also, by manipulating the supersaturation of the growth system, the equilibrium coefficient  $k_e$  and thus the solute partitioning function is affected to further influence the solute trapping as per  $k_e \propto \exp\left(-\frac{\Delta\mu}{RT}\right)$  seen above. Thus, the solute trapping of Sn in GeSn can be readily influenced by altering the kinetics of the growth system with the varied catalysts and precursors (as seen from the variation in Sn incorporation in Figure 3(c)). Other than the kinetic factors such as interfacial velocity and supersaturation, particularly for the Ge-Sn system, the incorporation of Sn is also aided by Sn’s negligible diffusion in Ge at the growth conditions, the epitaxial mismatch between Sn and Ge, the resulting elastic strain at the interface and the lack of truncating side facets at the seed-nanowire interface (which can act as attractive sites for Sn aggregation).<sup>12</sup>



Raman Spectroscopy, a powerful and non-destructive tool, was used for the quantitative and qualitative assessment of the alloy nanowires. Figure 4(a) shows the Raman spectra of bulk Ge, pure Ge nanowire and the  $\text{Ge}_{1-x}\text{Sn}_x$  nanowires incorporated with different concentrations of Sn. The measurements have been done on single nanowires and a very low laser power was used to avoid laser induced heating. For all of the samples the diameter of each measured nanowire is the same. The spectra are fitted with Lorentzian functions. In bulk, the Ge-Ge LO vibration is observed at  $303.3 \text{ cm}^{-1}$  whereas for the Ge NW this vibration shifts to  $302.7 \text{ cm}^{-1}$ , which is due to the phonon confinement effect. In GeSn alloy the Ge-Ge mode monotonically moves towards lower frequency (see Figure 4(b)) and shows asymmetry in the lower energy side of the spectrum due to the development of a Ge-Sn coupled vibrational mode<sup>43</sup> with increasing Sn concentration (as determined by EDX measurements). With Sn incorporation in the Ge lattice, both compositional variations and strain cause a shift of Ge-Ge LO mode compared to bulk Ge as well as from phase pure Ge nanowire. The shift coefficient of the Ge-Ge mode can be written as  $\Delta\omega = \omega(\text{SnGe}) - \omega(\text{Ge}) = \Delta\omega_{\text{composition}} + \Delta\omega_{\text{strain}}$ .<sup>44</sup> The compositional dependence of Ge-Ge Raman modes can be understood by the combined effect of mass disorder and bond distortion. Participation of compressive and tensile strain towards the Raman shift is not justified for nanowire samples, as due to the large surface area, strain can be effectively released for these nanostructures. Compressive strain may originate from the surface oxides in nanowires. But this strain shifts the Ge-Ge Raman mode of the Ge nanowire towards higher frequency compared to unstrained Ge, whereas in our Ge nanowire, we have observed only red shift in phase pure as well as Sn incorporated Ge nanowire with respect to the highly pure bulk Ge. This result exhibits that the oxide layer induced strain effect is non-significant for our Ge nanowire samples. Therefore, the total shift of Ge-Ge frequency is mainly attributed to the alloy disorder. We have fitted the Raman peak shift ( $\Delta\omega$ ) against Sn composition ( $x$ ), as determined through EDX analysis, with a linear expression  $\Delta\omega = ax$ , where  $a$  is a constant termed the alloy disorder coefficient.<sup>44</sup> For a fully relaxed  $\text{Ge}_{1-x}\text{Sn}_x$  alloy the theoretical value for the alloy disorder coefficient is calculated as  $95 \text{ cm}^{-1}$ .<sup>45</sup> From the linear shift of experimental data presented in Figure 4(b) the value obtained for the alloy disorder coefficient

was  $75.63 \text{ cm}^{-1}$  for the relaxed alloy nanowires. This is higher than the earlier report for  $\text{Ge}_{1-x}\text{Sn}_x$  nanowires,<sup>12</sup> where a smaller value ( $64.3 \text{ cm}^{-1}$ ) is attributed to a random alloying effect primarily in the nanowire sample with  $> 9 \text{ at.}\%$  Sn content. Apart from the Raman shift of the Ge-Ge mode a distinct increase in the half width at half maximum (HWHM) of Ge-Ge LO mode on the low energy side was observed with increasing Sn concentration as shown in Figure 4(c).

To further evaluate impurity ordering in the  $\text{Ge}_{1-x}\text{Sn}_x$  ( $x > 0.09$ ) alloy nanowires, we compared the Raman signal from  $9.14 \text{ at.}\%$  Sn incorporated alloy nanowires with  $\text{Ge}_{1-x}\text{Sn}_x$  nanowires where Sn is incorporated via a “two step” solute trapping and precipitation dissolution process.<sup>12</sup> As all of the nanowire samples are similar in diameter and exhibit a standard deviation of approximately  $\pm 1 \text{ at.}\%$  Sn from their mean Sn contents, the  $\text{Ge}_{1-x}\text{Sn}_x$  nanowires presented in this work can be compared to those in ref. 12. Both the Raman shift and the HWHM of the Ge-Ge phonon mode from the alloy nanowire in ref. 12 are included in Figure 4 (b) and (c) respectively. A clear downshift in the Raman frequency was observed for the alloy nanowire grown in this work compared with the nanowire grown via two-step process. The calculated alloy disorder coefficient for the particular nanowire ( $x = 0.091$ ) sample grown in this work is also much larger ( $93.2 \pm 4.1 \text{ cm}^{-1}$ ) than the alloy nanowire ( $x = 0.092$ ) grown in ref. 12 ( $62.4 \text{ cm}^{-1}$ ). In fact, the alloy disorder coefficient for the nanowire with  $9.1 \text{ at.}\%$  Sn; grown in this work is very near to the theoretical value for a perfectly relaxed  $\text{Ge}_{1-x}\text{Sn}_x$  alloy. Another interesting observation (Figure 4 (c)) is the much smaller low energy HWHM in case of alloy nanowires ( $9.2 \text{ at.}\%$  Sn) grown in ref. 12. A nanowire sample consisting of a mixture of partially ordered phase can lead to an apparent broadening of the low-energy half width of the Raman spectrum due to the appearance of additional Raman intensity at lower energies. The observation of large composition dependent Raman shift, high alloy disorder coefficient and a broad low-energy half width for the  $\text{Ge}_{1-x}\text{Sn}_x$  ( $x = 0.091$ ) nanowire implies an improvement in ordering of Sn via a single step inclusion process through trapping mechanism<sup>43,45</sup> when compared to previous work<sup>12</sup> where a two-step process was availed to encourage around  $9 \text{ at.}\%$  Sn incorporation. Deviation from a

perfectly random distribution and observation of short range ordering was previously observed through atom probe tomography in SiGeSn ternary alloy with > 4 at.% Sn content.<sup>20</sup>

The induction of impurity atoms into the nanowire lattice can induce defects at which impurities subsequently accumulate.<sup>46</sup> As such, it is imperative to determine the structural quality of the  $\text{Ge}_{1-x}\text{Sn}_x$  nanowires with large (> 9 at. %) Sn content. The dark field STEM images shown in Figure 5(a) display the single crystalline nature of the  $\text{Ge}_{1-x}\text{Sn}_x$  nanowires with the highest Sn incorporation (9.1 at. %). A high resolution STEM image recorded in HAADF mode from a particular area of the nanowire, highlighted with the blue coloured box, depicts the high crystallinity of the nanowire. Generally, the crystal structure of the  $\text{Ge}_{1-x}\text{Sn}_x$  alloy nanowires, with various Sn incorporations, exhibited a 3C lattice arrangement without any stacking faults and twin boundaries. Measuring the spacing between 50 successive layers of the nanowire, recorded with  $\langle 110 \rangle$  zone axis alignment, confirmed small fluctuation in the interplanar distance (Figure S10). This observation is in contrast with the large fluctuation in the interplanar spacing observed (Figure S10) for the  $\text{Ge}_{1-x}\text{Sn}_x$  nanowires; grown with two step process; with 9.2 at. % Sn incorporation, where a post-growth eutectic dissolution aided large Sn incorporation.<sup>12</sup> Relative order of atomic-scale randomness in  $\text{Ge}_{1-x}\text{Sn}_x$  alloy can generate varied local lattice distortion and spacing at an Ångström-level scale. Thus, small fluctuation of the interplanar spacing in the line profiles of the nanowires (Figure S10) suggests an improvement over the atomic ordering of Sn impurities in  $\text{Ge}_{1-x}\text{Sn}_x$  alloy lattice where Sn is incorporated via a single solute trapping mechanism rather than via a eutectic diffusion and solubility process. The mean interplanar spacing of 0.34 nm between  $\{111\}$  planes is observed from Fast Fourier Transform (FFT) analysis of the HR STEM, which agrees well with the  $d$  value for bulk diamond Ge crystal of 0.326 nm (JCPDS 04–0545). This slight increase in the  $d$  spacing is to be expected upon the incorporation of Sn into the Ge host lattice due to the difference in the lattice constants of Ge and Sn which can instigate a lattice expansion. The nanowires predominantly displayed  $\langle 111 \rangle$  as the growth direction which is the most common growth orientation for Ge nanowires with mean

diameter above 50 nm.<sup>12,26</sup> Further TEM (Supporting Info, Figure S11) studies on Ge<sub>1-x</sub>Sn<sub>x</sub> verified that the nanowires were defect free with <111> as the dominant growth direction.

To confirm the sparse and uniform distribution of Sn in the Ge lattice of the nanowires, we probed the spatial arrangement of Sn through energy electron loss spectroscopy (EELS). EELS mapping was carried out in low resolution HAADF STEM mode. HAADF and the corresponding EELS chemical profile recorded from the rectangular box region are depicted in Figure 5(b). EELS spectral images are recorded for Sn  $M_{4,5}$  (red) and Ge  $L_{2,3}$  (green) edges and highlight the incorporation of Sn in the Ge nanowire core. The sharp contrast between the Sn rich seed and the nanowire body is visible in the HAADF image and in the EELS spectral images for Ge and Sn. No Sn clustering and segregation in the bulk of the nanowire, or sidewall precipitation of metallic Sn, was observed from the EELS spectral images. A deformed catalyst, a phase segregated largely amorphous “bulb” around a highly contrasted metallic seed, at the tip of the nanowire was also observed via TEM (see Supporting Info, Figure S11) and HAADF STEM analysis (Figure 5(b)). EDX elemental mapping on this “bulb” region revealed that the composition of this amorphous region was less Sn rich than the seed it surrounded (40-50 at. % Sn in the amorphous region compared to ~80 at. % in the actual hemispherical catalyst). The EELS spectral image corresponding to Sn also confirmed the phase segregated amorphous region to be less Sn rich than the actual growth seed (Figure 5(b)). Although EELS, EDX and Raman analysis verify the quality (uniformity, ordering etc.) of Sn distribution in the Ge lattice, atomic scale study such as atom probe tomography<sup>20</sup> is required to provide deeper insights into the distribution of Sn in non- equilibrium Ge<sub>1-x</sub>Sn<sub>x</sub>.

Ge is a good candidate for achieving a direct bandgap by alloying with Sn as there is only a small energy separation of 140 meV between the indirect (L) and direct ( $\Gamma$ ) valleys in the conduction band. Photoluminescence (PL) is a primary technique to determine the nature of the bandgap in nanoscale alloy

systems.<sup>11,47–50</sup> The linewidths of the PL spectra, as well as peak position, give invaluable insight into the nature of the electronic transition. To examine the nature of the band transition of  $\text{Ge}_{1-x}\text{Sn}_x$  nanowires, low temperature PL studies were carried out using a liquid nitrogen cryostat. A PL spectrum taken at 80 K using a Ti:Sa laser with 950 nm wavelength was obtained for the nanowires with 9.1 at. % Sn (Figure 6(a) black line). The PL spectrum for the 9.1 at. % Sn incorporated alloy nanowire shows a single peak centred at 2046 nm, which equates to a band gap energy of 0.61 eV. By fitting the spectra to a GaussAmp function, the full width half maximum (FWHM) was obtained. The emission has a relatively narrow linewidth of 220 nm. A PL spectrum recorded at 80 K for the  $\text{Ge}_{1-x}\text{Sn}_x$  nanowire with  $x = 0.07$  also displayed a red-shifted single peak which was centred at 1875 nm, or 0.66 eV (Figure 6(a) red line). Comparatively, this peak had a notably broad linewidth of 617 nm. This broad linewidth could be due to the indirect nature of the band transition. At this Sn content separate peaks due to direct and indirect transition cannot be identified due to the reduced energy difference between direct and indirect bandgap, resulting in a single peak with a broad linewidth.

Additionally, temperature dependent PL studies are also an invaluable data set in proving the nature of a bandgap<sup>4,51</sup>. Temperature dependent PL studies have previously been used to prove the direct nature of  $\text{Ge}_{1-x}\text{Sn}_x$  materials<sup>4,12,52,53</sup>. The nature of the bandgap was verified by the temperature dependent studies from 80 K – 300 K. PL temperature mapping contour plot of  $\text{Ge}_{1-x}\text{Sn}_x$  ( $x = 0.074$ ) nanowires showed a decrease in PL intensity with decreasing the temperature up to 80K (Figure 6(b), further spectral plots in Supporting Information, Figure S12). The room-temperature PL originating from electron–hole recombination at the centre of the Brillouin zone ( $\Gamma$ -point) should decrease in intensity with decreasing temperature for a typical indirect bandgap semiconductor.<sup>54,55</sup> The increase in the PL intensity with increasing temperature is due to the thermally activated electron located in the L-valley populating the  $\Gamma$  valley leading to increase in the PL intensity.<sup>55</sup> An uncommon small blue shift of the PL emission with increasing temperature (Figure 6(b)), which is untypical of semiconductors, was observed for 7.4 at. %

Sn incorporated  $\text{Ge}_{1-x}\text{Sn}_x$  nanowires. Ionization of deep impurity levels into the band gap could result in a blue shift in the PL peak with increasing temperature.<sup>56</sup> However blue-shift originating from this effect usually occurs at low temperatures ( $<100$  K), as after the activation of deep impurity levels at higher temperature the PL peak starts to red-shift as is the case with typical semiconductors. In  $\text{Ge}_{1-x}\text{Sn}_x$  ( $x = 0.074$ ) nanowires, due to the very small difference between the direct and indirect bandgap, the direct transition becomes very close to the indirect and becomes dominant with increasing temperature due to shorter charge carrier lifetimes. In indirect materials close to the indirect-to-direct crossover point, with the rise of temperatures, transitions from both the L &  $\Gamma$  valley can be observed.<sup>51</sup> This explains the uncommon blue shift of emission with increasing temperature (Figure 6(b) and Supporting Information, Figure S12).<sup>53</sup> The observation of broad PL emission at low temperature and an uncommon increase in the bandgap energy with increasing temperature indicates that the  $\text{Ge}_{1-x}\text{Sn}_x$  nanowires with 7.4 at. % Sn incorporation is very close to the transition point where GeSn becomes a direct bandgap material. The transition from indirect to direct bandgap could be gradual, due to a degree of band overlap resulting from the narrow energy difference between the direct and indirect bands. Similar behaviour is reported for GeSn thin films,<sup>57</sup> as well as pure Ge films and nanowires.<sup>58–60</sup>

Temperature dependent PL studies were also carried out from 80 to 200 K on the  $\text{Ge}_{1-x}\text{Sn}_x$  nanowires with 9.1 at. % Sn. The variation in the PL intensity with temperature is depicted in the temperature map in Figure 6(c). PL spectra recorded at different temperatures can also be found in Supporting Information (Figure S12). A comparison of integrated intensity and band energy as a function of temperature is depicted in Figure S13 in Supporting Information for further clarity. The PL intensity decreases with increasing temperature, which can be attributed to a reduced transfer of electrons from the  $\Gamma$  to L valleys by thermal activation.<sup>53</sup> Thus the increase in the intensity of the PL peak with decreasing temperature for  $\text{Ge}_{1-x}\text{Sn}_x$  ( $x = 0.091$ ) nanowires samples is attributed to the higher population of the  $\Gamma$  valley. With increasing temperature the fast diffusion of photocarriers toward surfaces and interfaces leads to non-

radiative surface and interface recombination respectively, reducing the radiative transition rate with activation energy  $E_A$ . Non-radiative surface recombination generates a number of phonons and can occur in both 7.4 and 9.1 at. % Sn content  $\text{Ge}_{1-x}\text{Sn}_x$  nanowire. However, it has different effects on indirect and direct band-gap materials. In the case of 7.4 at. % Sn incorporated nanowires, phonons are required for recombination and its high concentration makes PL from phonon-assisted L-valley brighter at higher temperatures. Whereas for  $\text{Ge}_{1-x}\text{Sn}_x$  ( $x = 0.091$ ) nanowires phonons do not participate in the radiative recombination process and thus non-radiative channels result in the loss of electron-hole pairs on the surface. The activation energy  $E_A$  of non-radiative process at higher temperature was obtained as 16 meV from an Arrhenius plot (Supporting Information, Figure S14) for the  $\text{Ge}_{1-x}\text{Sn}_x$  nanowires with 9.1 at. % Sn. Decrease in the PL intensity with increase in temperature; which is typical behaviour of a direct bandgap III-V, dichalcogenides and IV-VI semiconductor,<sup>4,12,51,52,54</sup> and the activation energy value comparable to the direct band gap compressively strained GeSn alloys<sup>47</sup> confirms the direct bandgap for  $\text{Ge}_{1-x}\text{Sn}_x$  nanowires with 9.1 at.% Sn incorporation. It is apparent that the nature of the bandgap in the  $\text{Ge}_{1-x}\text{Sn}_x$  nanowires has changed significantly, from near direct to direct, with the increase in amount of Sn in the alloy by merely 1.6 at. %. Though the steady state PL measurements gave an indication on the nature of the band gap for  $\text{Ge}_{1-x}\text{Sn}_x$  alloy, direct measurements of the carrier lifetime are required in order to precisely resolve the directness of the electronic band structure.

In order to explore the effect of alloy ordering on the band structure of  $\text{Ge}_{1-x}\text{Sn}_x$  nanowires, it is important to iterate the dependence of the photoluminescence on the alloy disorder. Optically, this change in the fundamental bandgap and band structure can be observed through the photoluminescence line width.<sup>61,62</sup> The electronic states near to the conduction band edge and the valence band edges could be strongly affected by the alloy ordering which translates into an intrinsically higher inhomogeneous broadening of PL emission.<sup>63,64</sup> The consequence of short-range alloy ordering on the PL is apparent from the observation of the narrow line-width for the emission (Figure 6 (a)) from spontaneously, comparatively ordered  $\text{Ge}_{1-x}\text{Sn}_x$  ( $x = 0.091$ ) nanowires, as determined from Raman analysis. The emission from the alloy

nanowires synthesised in this work with > 9 at.% Sn is significantly narrower than that from the randomly ordered  $\text{Ge}_{1-x}\text{Sn}_x$  nanowires.<sup>12</sup> PL spectrum recorded at 80 K from the randomly ordered  $\text{Ge}_{1-x}\text{Sn}_x$  nanowires fabricated by a two-step process (Supporting Info., Figure S15) has a line-width of 761 nm. This is significantly (3.5 times) broader than the PL emission from the more spontaneously ordered alloy nanowire synthesized in this work; with a similar Sn incorporation grown via single step VLS process. Apart from the PL line width, a significant increase in the activation energy ( $E_A$ ) for non-radiative process is observed for the ordered  $\text{Ge}_{1-x}\text{Sn}_x$  ( $x = 0.091$ ) nanowires (16 meV) compared to  $\text{Ge}_{1-x}\text{Sn}_x$  ( $x = 0.092$ ) nanowire (7 meV) with random Sn distribution.<sup>12</sup> An increase in the activation energy with increasing degree of ordering was also observed for III-V semiconductors.<sup>21,65</sup> It has been suggested that as  $E_A$  for the non-radiative process represents the barrier between the ordered domains and disordered domain containing the non-radiative centres, an increase in  $E_A$  signifies higher degree of ordering in the semiconductor.<sup>65,66</sup> Although the current PL measurements indicate improved emission in terms of line width from the alloy nanowire with enhanced short-range ordering of impurity, further confirmation regarding the effect of alloy ordering on the bandgap and light emission is required, *e.g.* including radiative rates and quantum efficiencies.

Furthermore, to confirm the nature of the bandgap in the alloy nanowires, EELS analysis was carried out on  $\text{Ge}_{1-x}\text{Sn}_x$  nanowires with 9 at. % Sn using a Nion UltraSTEM at high resolution. Background subtraction (red line) of the EELS spectrum (blue line) was achieved by taking the zero loss peak, resulting in a spectrum denoted by the green line seen shown in Figure 6(d).<sup>67,68</sup> The onset (an enlarged view of the sub 1.0 eV region can be found in Supporting Information (Figure S16)) of the spectrum (green line) was used to determine the value of the bandgap energy ( $E_g$ ). The EELS spectrum shows a transition at 0.61 – 0.62 eV, which agrees well with the bandgap energy determined from the PL study shown in Figure 6(a). The shape of the EELS curve also provides information about the nature of the transition. For a direct transition, an  $(E - E_g)^{1/2}$  term is observed in the spectrum, an  $(E - E_g)^{3/2}$  term determines the shape



of the spectrum for an indirect transition.<sup>69,70</sup> Therefore, the nature of the transition can be easily determined from the shape of the spectrum which is produced. The parabolic shape of the curve between  $\sim 0.58$  eV and  $\sim 1.8$  eV indicates a direct transition, while the hyperbolic curve which succeeds this is typical of an indirect transition. These curves are indicated in Figure 6(d) with the turning point of the curve denoted by the dark green dashed line.

## Conclusion

Varying the growth parameters to influence the kinetics of the  $\text{Ge}_{1-x}\text{Sn}_x$  system can dramatically impact Sn uptake in the nanowires. By exploring the effects of temperature, precursor and catalyst an optimal growth regime was explored to obtain high growth kinetics of  $\text{Ge}_{1-x}\text{Sn}_x$  nanowires. By using tetraethyltin as the Sn source and varying the composition of the AuAg alloy catalyst, morphologically uniform and crystalline nanowires with homogeneous Sn incorporation of  $> 9$  at. % were obtained with an  $\text{Au}_{0.80}\text{Ag}_{0.20}$  catalyst. Longer  $\text{Ge}_{1-x}\text{Sn}_x$  nanowires were more Sn rich than the shorter  $\text{Ge}_{1-x}\text{Sn}_x$  nanowires, establishing a relationship between growth kinetics and Sn incorporation. Faster growth rates resulted in nanowires with higher Sn incorporation, confirming the participation of a kinetic dependence of the solute trapping for Sn incorporation. The understanding of the role of the growth constraint and growth kinetics in the VLS process in Sn impurity incorporation in GeSn nanowires could contribute towards the development of group IV alloys with different stoichiometry and also other new functional alloy materials. For example, a further manipulation in Sn content in  $\text{Ge}_{1-x}\text{Sn}_x$  nanowires can be expected with the introduction and variation of new parameters such as catalyst concentration or pressure.

The  $\text{Ge}_{1-x}\text{Sn}_x$  nanowires with  $x = 0.09$  were determined to be direct bandgap from both PL and EELS analysis. An indirect to direct transition point was identified for the nanowires between 7 and 9 at. % of Sn incorporation. Enhanced spontaneous ordering of Sn impurities, as detected via Raman spectroscopy, resulted in a sharp direct band gap emission from the  $\text{Ge}_{1-x}\text{Sn}_x$  nanowires with  $x = 0.09$ . More knowledge

on the effect of qualitative distribution of the foreign atoms in the host semiconductor lattice via complemented atomic scale mapping (e.g. atom probe tomography) and advance optical analysis will allow exploration of novel properties such as nanoscale strain engineering, controlled defect formation, band structure modulation in the existing nanoscale group IV alloy semiconductor architecture. The fabrication of direct bandgap  $\text{Ge}_{1-x}\text{Sn}_x$  nanowires with high Sn content ( $> 9$  at. %) demonstrates a low cost, silicon compatible solution to the ongoing demand for nanoscale group IV photonics via a conventional catalytic approach. These direct bandgap  $\text{Ge}_{1-x}\text{Sn}_x$  nanowires, with narrow emission widths, a uniform morphology, high crystallinity and homogeneous Sn distribution, demonstrate themselves to be suitable candidates for implementation in photonic and optoelectronic devices.

### **Electronic Supplementary information**

Supplementary material containing EDX analysis of GeSn nanowires, additional TEM images and analysis, detail on the nanoparticle catalysts and photoluminescence from 7.4 at.% Sn containing GeSn nanowire is available in the online version of this article at [http://dx.doi.org/10.1007/\\*\\*\\*\\*\\*](http://dx.doi.org/10.1007/*****)

### **Author Contributions**

J.D. co-wrote the paper with S.B, and performed experiments on nanowire growth. S.B. and J.D.H planned the experiments. D.S. and T.P. performed photoluminescence measurements whereas A.S. and T.B. performed Raman spectroscopy on GeSn nanowires samples. J.D.H. led overall effort and co-wrote the paper. All authors discussed and commented on the manuscript and on the results.

### **Acknowledgements**

This research was funded by Science Foundation Ireland (Grant No: 14/IA/2513 & US -Ireland R&D Partnership Program Grant No. SFI/14/US/I3057), and by the Irish Research Council through a Postgraduate Scholarship to JD (Grant No.: GOIPG/2015/2772). We would like to acknowledge the Advanced Microscopy Laboratory, Trinity College Dublin, for their contribution to the imaging.

## **Conflicts of interest**

Authors declare no conflict of interest.

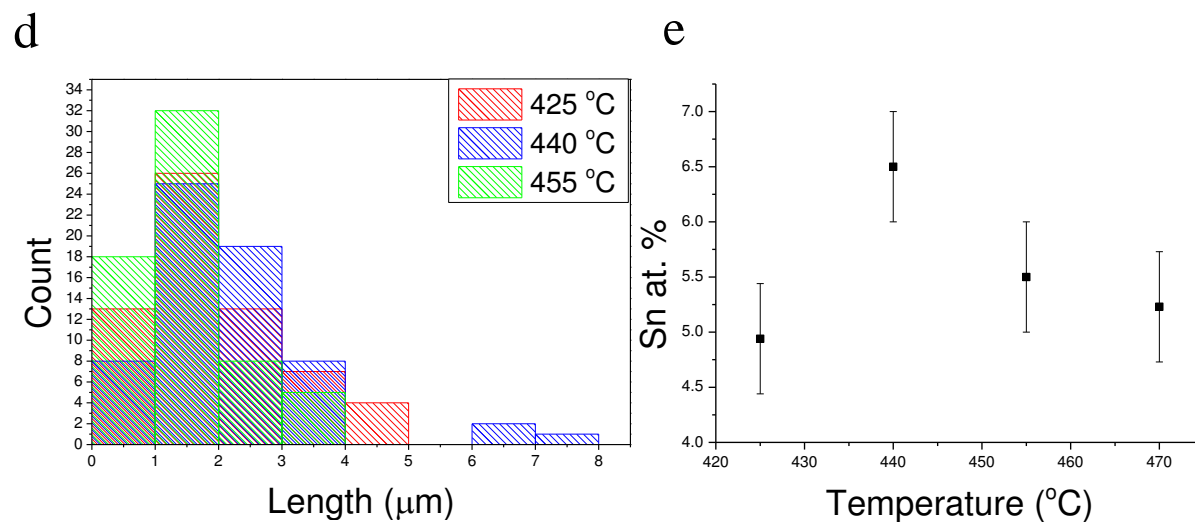
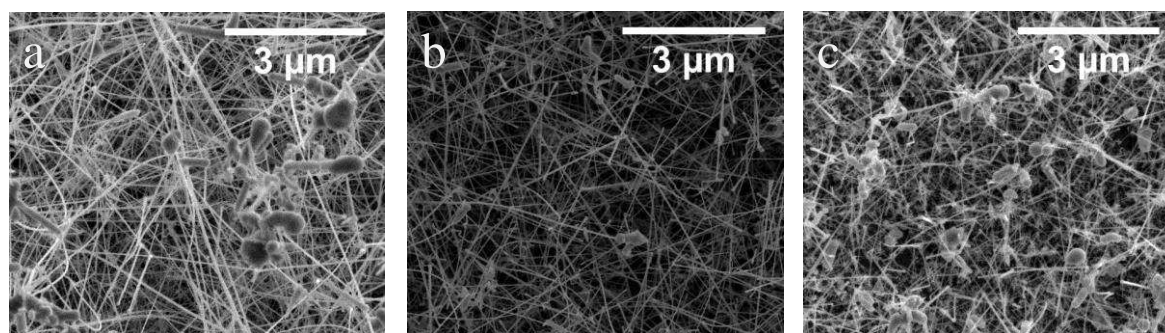


Figure 1. SEM images of Ge<sub>1-x</sub>Sn<sub>x</sub> nanowires grown using ATBS as the Sn source, catalysed by Au<sub>0.90</sub>Ag<sub>0.10</sub> nanoparticles at (a) 425 °C, (b) 440 °C and (c) 455 °C. (d) Nanowire length distributions for each sample. Plot in part (e) displays the varying Sn incorporation with temperature. Error bars represent the typical error of 0.5 at. % in EDX elemental measurements.

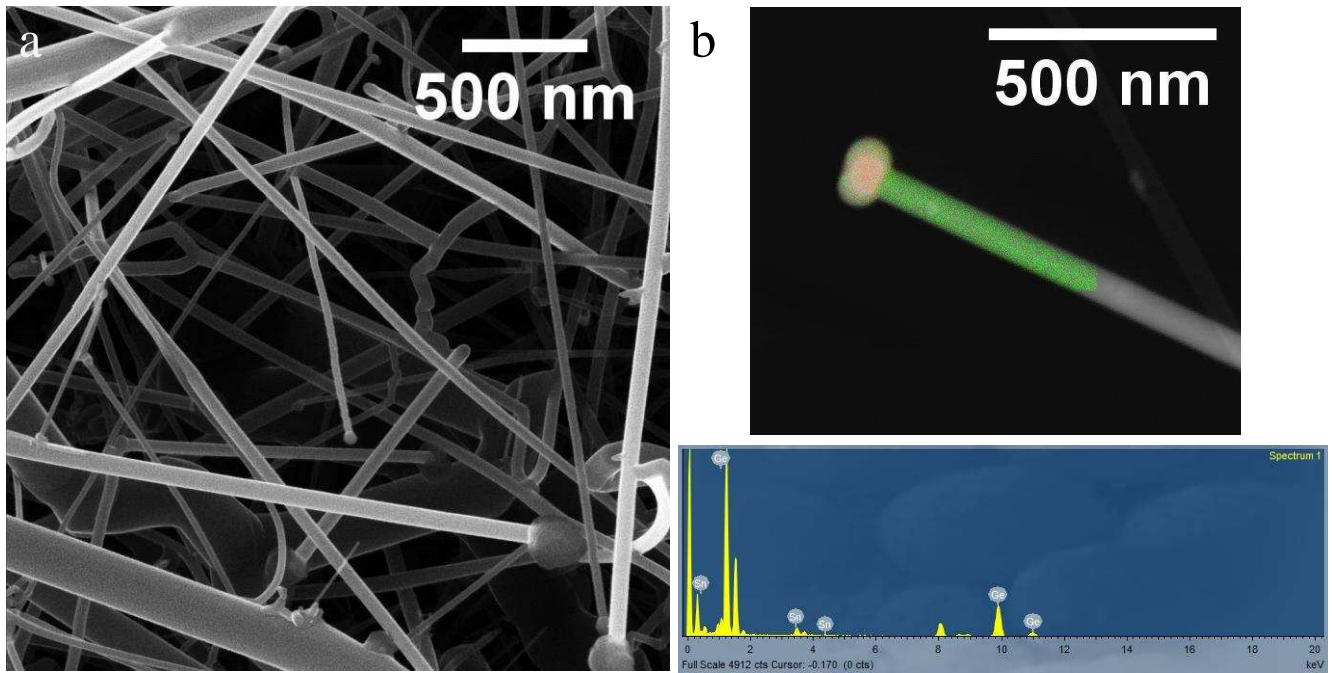


Figure 2: (a) Helium ion microscope (HIM) image of  $\text{Ge}_{1-x}\text{Sn}_x$  nanowires with average Sn content of 8.7 at. %, synthesised with TET with  $\text{Au}_{0.90}\text{Ag}_{0.10}$  nanoparticles as growth promoters. Part shows a (b) single nanowire EDX elemental map with corresponding spectra: Sn is denoted by red and Ge by green, demonstrating the homogeneous distribution of Sn in the nanowire.

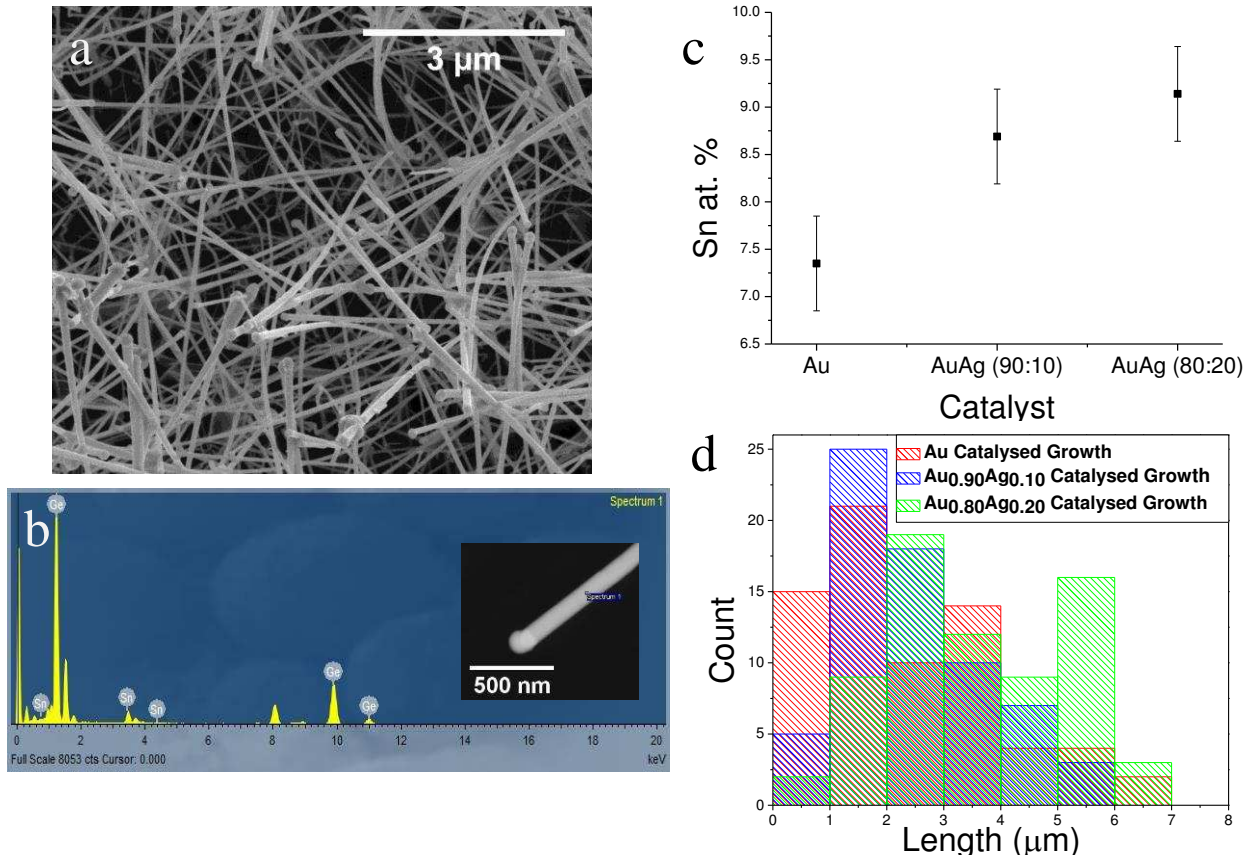


Figure 3: (a) SEM image of  $\text{Ge}_{1-x}\text{Sn}_x$  nanowires grown using TET as a Sn source, catalysed by  $\text{Au}_{0.80}\text{Ag}_{0.20}$  nanoparticles. EDX analysis in (b) confirms the high Sn incorporation ( $x = 0.091$ ). A graph demonstrating the increase in the amount of Sn incorporated into the nanowires with increasing Ag in the nanoparticle catalyst can be seen in (c). Error bars represent the typical error of 0.5 at. %. The length distributions of these samples in (d) show the increase in the mean nanowire length with increasing Ag content in the nanoparticle catalyst.

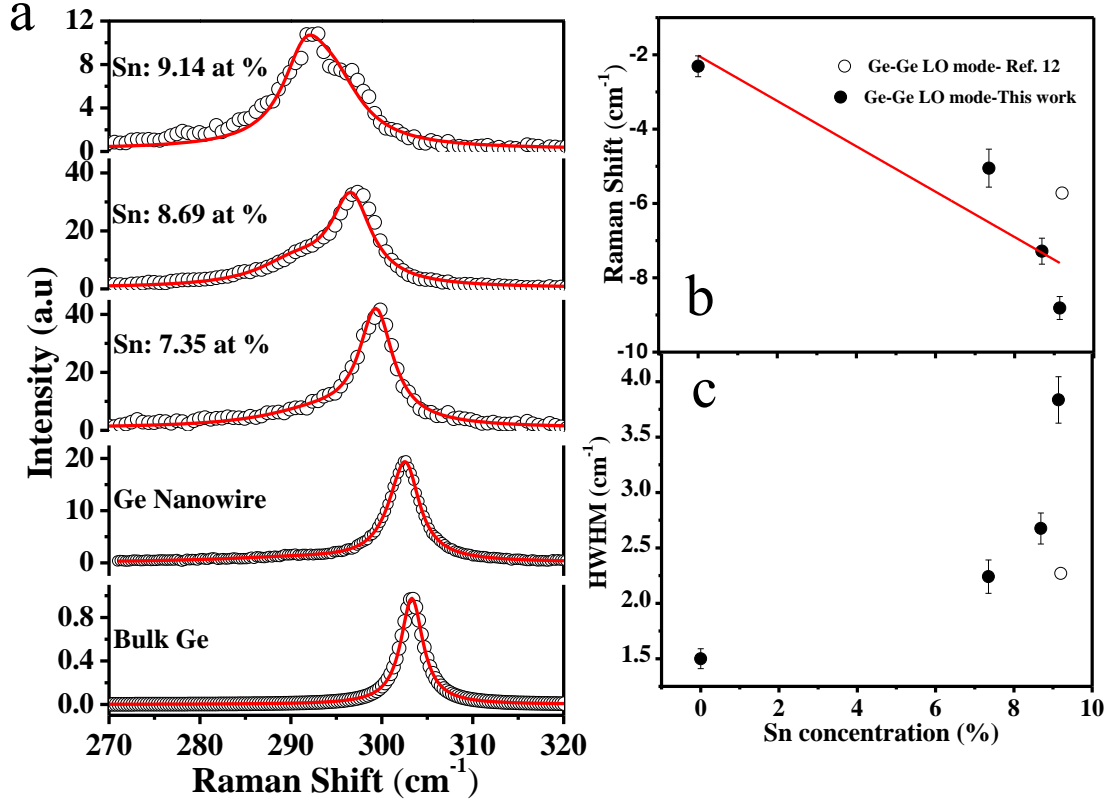


Figure 4: (a) Room temperature Raman spectrum for the Ge–Ge mode in  $\text{Ge}_{1-x}\text{Sn}_x$  alloy nanowires (where  $x$  varies from 0.07 to 0.09). (b) The downshift of Ge-Ge LO mode and (c) the HWHM of the Raman peak for the Ge–Ge mode of Ge-Sn alloy nanowires with Sn percentage variation. Experimental data are represented with dots which fits (straight line) well with the linear expression,  $\Delta\omega = ax$ . Black dots represent the characteristics of Ge-Ge LO mode of present study; white dots represent the Ge–Ge mode of  $\text{Ge}_{1-x}\text{Sn}_x$  nanowire grown with a two step process<sup>12</sup>. Error bars indicate the error associated with the instrumental resolution and fitting. The excitation wavelength is 488 nm.

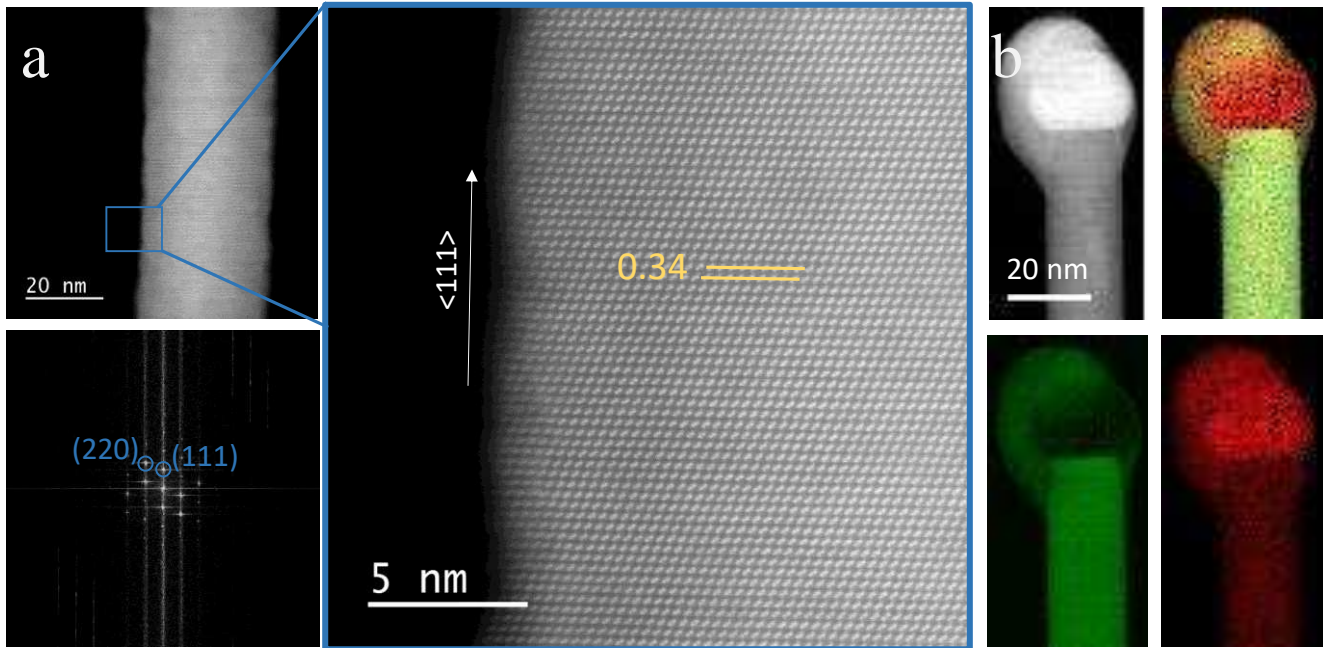


Figure 5: (a) High resolution STEM image of a  $\text{Ge}_{1-x}\text{Sn}_x$  nanowire with an average 9.1 at. % Sn. FFT confirms the formation for Ge-like diamond cubic  $\text{Ge}_{1-x}\text{Sn}_x$  crystal. This is also verified by lattice spacing measured for 50 successive planes. The nanowires are single crystalline with no apparent defects. EELS mapping in (b) displays the sharp interface between the catalyst seed and the nanowire body. Sn is denoted by red and Ge by green. Also a Sn rich GeSn phase segregated extension with “bulb” shape is observed around the seed.



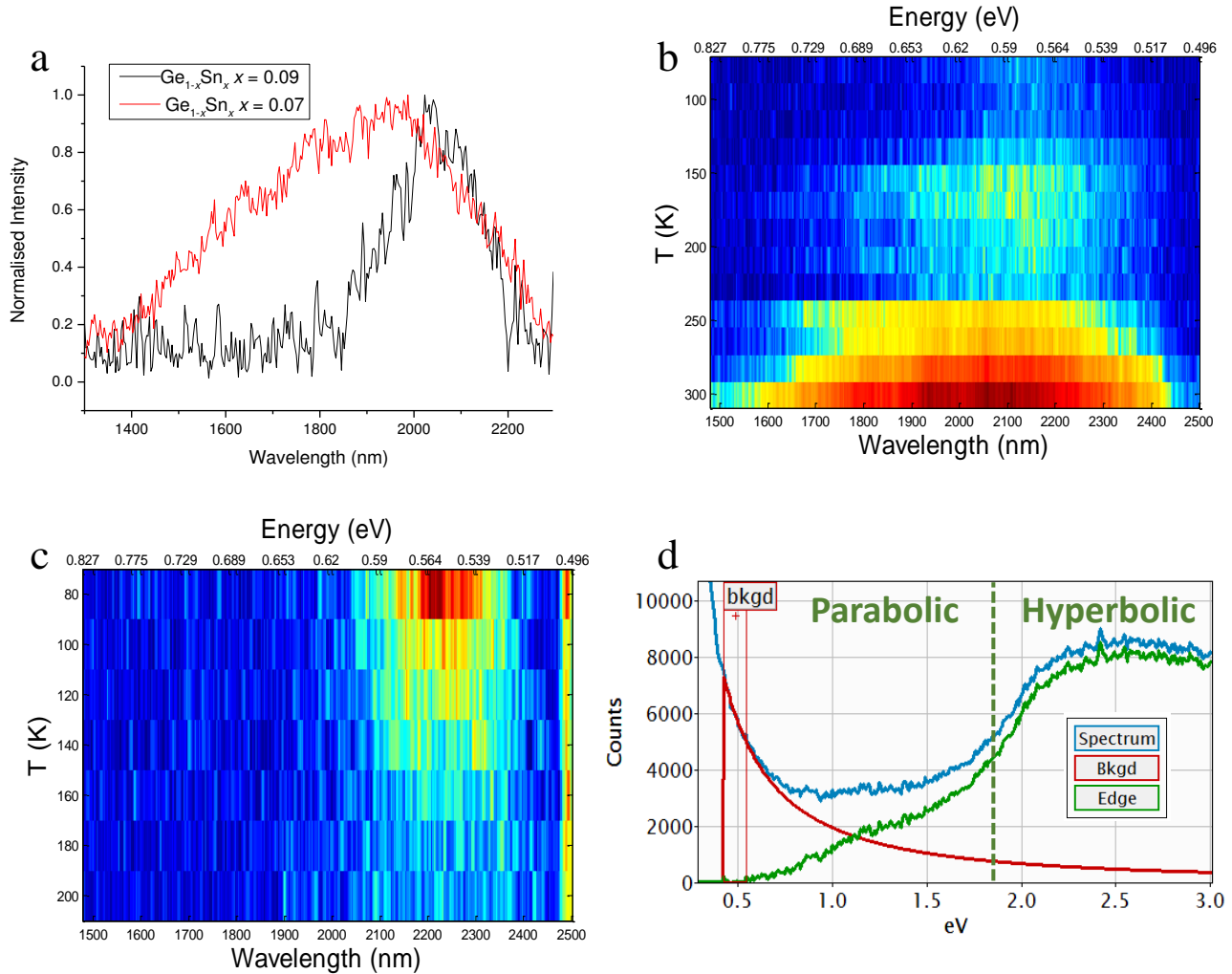


Figure 6: (a) Photoluminescence spectra for Ge<sub>1-x</sub>Sn<sub>x</sub> nanowires with 9.1 at. % Sn showing a narrow emission at 2046 nm (0.61 eV) at 80 K (black line) and Ge<sub>1-x</sub>Sn<sub>x</sub> nanowires with 7.4 at. % Sn showing much broader emission at 1875 nm (0.66 eV). Temperature dependent studies in part (b) and (c) confirm the bandgap transition for the indirect ( $x = 0.074$ ) nanowires and direct bandgap transition of the Ge<sub>1-x</sub>Sn<sub>x</sub> nanowires with  $x = 0.091$ . The contour plot in (b) shows a direct relationship between temperature and intensity, characteristic of an indirect bandgap material. Contrarily, (c) displays a decreasing intensity with increasing temperature, indicative of a direct bandgap material. (d) EEL spectra of a Ge<sub>1-x</sub>Sn<sub>x</sub> nanowire with 9.1 at. % Sn. The green line begins to rise at approx. 0.6 eV, indicating a bandgap at that energy. The parabolic nature of the green curve to the green dashed line is indicative of a direct transition.

## REFERENCES

- 1 a. T. Fiory and N. M. Ravindra, *J. Electron. Mater.*, 2003, **32**, 1043–1051.
- 2 A. M. Ionescu and H. Riel, *Nature*, 2011, **479**, 329–337.
- 3 C. Schulte-Braucks, S. Glass, E. Hofmann, D. Stange, N. Von Den Driesch, Q. T. Zhao, D. Buca, S. Mantl, J. M. Hartmann and Z. Ikonc, 2016 *Jt. Int. EUROSOI Work. Int. Conf. Ultim. Integr. Silicon, EUROSOI-ULIS 2016*, 2016, **9**, 24–27.
- 4 S. Wirths, R. Geiger, N. V. Den Driesch, G. Mussler, T. Stoica, S. Mantl, Z. Ikonc, M. Luysberg, S. Chiussi, J. M. Hartmann, H. Sigg, J. Faist, D. Buca and D. Grützmacher, 2015, 1–5.
- 5 S. Al-Kabi, S. A. Ghetmiri, J. Margetis, T. Pham, Y. Zhou, W. Dou, B. Collier, R. Quinde, W. Du, A. Mosleh, J. Liu, G. Sun, R. A. Soref, J. Tolle, B. Li, M. Mortazavi, H. A. Naseem and S. Q. Yu, *Appl. Phys. Lett.*, , DOI:10.1063/1.4966141.
- 6 R. Soref, *Nat. Photonics*, 2010, **4**, 495–497.
- 7 J. D. Sau and M. L. Cohen, *Phys. Rev. B - Condens. Matter Mater. Phys.*, 2007, **75**, 1–7.
- 8 D. Jenkins and J. Dow, *Phys. Rev. B*, 1987, **36**, 7994–8000.
- 9 V. Richard D’Costa, W. Wang, Q. Zhou, E. Soon Tok and Y. C. Yeo, *Appl. Phys. Lett.*, , DOI:10.1063/1.4862659.
- 10 Q. T. Zhao, S. Richter, C. Schulte-Braucks, L. Knoll, S. Blaeser, G. V. Luong, S. Trelenkamp, A. Schafer, A. Tiedemann, J. M. Hartmann, K. Bourdelle and S. Mantl, *IEEE J. Electron Devices Soc.*, 2015, **3**, 103–114.
- 11 S. Assali, A. Dijkstra, A. Li, S. Koelling, M. A. Verheijen, L. Gagliano, N. Von Den Driesch, D. Buca, P. M. Koenraad, J. E. M. Haverkort and E. P. A. M. Bakkers, *Nano Lett.*, 2017, **17**, 1538–1544.
- 12 S. Biswas, J. Doherty, D. Saladukha, Q. Ramasse, D. Majumdar, M. Upmanyu, A. Singha, T. Ochalski, M. A. Morris and J. D. Holmes, *Nat. Commun.*, 2016, **7**, 11405.
- 13 R. Ragan, C. C. Ahn and H. a. Atwater, *Appl. Phys. Lett.*, 2003, **82**, 3439–3441.
- 14 S. Gupta, R. Chen, Y. C. Huang, Y. Kim, E. Sanchez, J. S. Harris and K. C. Saraswat, *Nano Lett.*,

- 2013, **13**, 3783–3790.
- 15 M. S. Seifner, F. Biegger, A. Lugstein, J. Bernardi and S. Barth, *Chem. Mater.*, 2015, **27**, 6125–6130.
- 16 E. Mullane, T. Kennedy, H. Geaney, C. Dickinson and K. M. Ryan, *Chem. Mater.*, 2013, **25**, 1816–1822.
- 17 M. S. Seifner, S. Hernandez, J. Bernardi, A. Romano-Rodriguez and S. Barth, *Chem. Mater.*, 2017, [acs.chemmater.7b03969](https://doi.org/10.1021/acs.chemmater.7b03969).
- 18 P. Galenko, *Phys. Rev. E - Stat. Nonlinear, Soft Matter Phys.*, 2007, **76**, 1–9.
- 19 K. Glasner, *Phys. D Nonlinear Phenom.*, 2001, **151**, 253–270.
- 20 S. Mukherjee, N. Kodali, D. Isheim, S. Wirths, J. M. Hartmann, D. Buca, D. N. Seidman and O. Moutanabbir, *Phys. Rev. B*, 2017, **95**, 1–5.
- 21 J. D. Lambkin, L. Considine, S. Walsh, G. M. O’Connor, C. J. McDonagh and T. J. Glynn, *Appl. Phys. Lett.*, 1994, **65**, 73–75.
- 22 G. Wagner, K. Richter and P. Paufler, *Phys. Rev. B - Condens. Matter Mater. Phys.*, 1999, **59**, 15253–15260.
- 23 A. Mascarenhas, S. Kurtz, A. Kibbler and J. M. Olson, *Phys. Rev. Lett.*, 1989, **63**, 2108–2111.
- 24 O. Moutanabbir, D. Isheim, H. Blumtritt, S. Senz, E. Pippel and D. N. Seidman, *Nature*, 2013, **496**, 78–82.
- 25 S. Biswas, C. O’Regan, M. a. Morris and J. D. Holmes, *Small*, 2015, **11**, 103–111.
- 26 S. Biswas, C. O’Regan, N. Petkov, M. a. Morris and J. D. Holmes, *Nano Lett.*, 2013, **13**, 4044–4052.
- 27 S. T. He, S. S. Xie, J. N. Yao, H. J. Gao and S. J. Pang, *Appl. Phys. Lett.*, 2002, **81**, 150–152.
- 28 E. I. Givargizov, *J. Cryst. Growth*, 1975, **31**, 20–30.
- 29 S. A. Dayeh and S. T. Picraux, *Nano Lett.*, 2010, **10**, 4032–4039.
- 30 V. Schmidt, S. Senz and U. Gösele, *Phys. Rev. B - Condens. Matter Mater. Phys.*, 2007, **75**, 1–6.
- 31 S. Biswas, A. Singha, M. a. Morris and J. D. Holmes, *Nano Lett.*, 2012, **12**, 5654–5663.

- 32 H.-J. Yang and H.-Y. Tuan, *J. Mater. Chem.*, 2012, **22**, 2215.
- 33 J. Aubin and J. M. Hartmann, *J. Cryst. Growth*, 2018, **482**, 30–35.
- 34 T. S. S. Wirths, D. Buca, A.T. Tiedemann, B. Holländer, P. Bernardy and and S. M. D. Grützmacher, *ECS Trans.*, 2012, **50**, 885–893.
- 35 D. C. Lee, T. Hanrath and B. A. Korgel, *Angew. Chemie - Int. Ed.*, 2005, **44**, 3573–3577.
- 36 C. O'Regan, S. Biswas, C. O'Kelly, S. J. Jung, J. J. Boland, N. Petkov and J. D. Holmes, *Chem. Mater.*, 2013, **25**, 3096–3104.
- 37 R. Reitano, P. M. Smith and M. J. Aziz, *J. Appl. Phys.*, 1994, **76**, 1518–1529.
- 38 S. Huang, Y. Wu, X. Zhu, L. Li, Z. Wang, L. Wang and G. Lu, *J. Appl. Phys.*, 2011, **109**, 1–6.
- 39 S. Rackauskas, H. Jiang, J. B. Wagner, S. D. Shandakov, T. W. Hansen, E. I. Kauppinen and A. G. Nasibulin, .
- 40 D. Zentrum, 2011, 457–466.
- 41 H. Assadi and a. L. Greer, *J. Cryst. Growth*, 1997, **172**, 249–258.
- 42 P. Kringhoj and R. G. Elliman, *Appl. Phys. Lett.*, 1994, **65**, 324–326.
- 43 S. F. Li, M. R. Bauer, J. Menéndez and J. Kouvetakis, *Appl. Phys. Lett.*, 2004, **84**, 867–869.
- 44 S. Su, W. Wang, B. Cheng, W. Hu, G. Zhang, C. Xue, Y. Zuo and Q. Wang, *Solid State Commun.*, 2011, **151**, 647–650.
- 45 R. Cheng, W. Wang, X. Gong, L. Sun, P. Guo, H. Hu, Z. Shen, G. Han and Y.-C. Yeo, *ECS J. Solid State Sci. Technol.*, 2013, **2**, P138–P145.
- 46 E. R. Hemesath, D. K. Schreiber, E. B. Gulsoy, C. F. Kisielowski, A. K. Petford-Long, P. W. Voorhees and L. J. Lauhon, *Nano Lett.*, 2012, **12**, 167–171.
- 47 S. A. Ghetmiri, W. Du, J. Margetis, A. Mosleh, L. Cousar, B. R. Conley, A. Nazzal, G. Sun, R. a Soref, J. Tolle, B. Li, H. a Naseem, S. A. Ghetmiri, W. Du, J. Margetis, A. Mosleh, L. Cousar, J. Tolle, B. Li, H. a Naseem and S. Yu, , DOI:10.1063/1.4898597.
- 48 J. Mathews, R. T. Beeler, J. Tolle, C. Xu, R. Roucka, J. Kouvetakis and J. Meéndez, *Appl. Phys. Lett.*, 2010, **97**, 2–5.

- 49 A. Mosleh, S. A. Ghetmiri, B. R. Conley, M. Hawkrige, M. Benamara, A. Nazzal, J. Tolle, S. Q. Yu and H. a. Naseem, *J. Electron. Mater.*, 2014, **43**, 938–946.
- 50 H. Dumont, L. Auvray and Y. Monteil, *Opt. Mater. (Amst.)*, 2003, **24**, 309–314.
- 51 D. Stange, S. Wirths, N. Von Den Driesch, G. Mussler, T. Stoica, Z. Ikonc, J. M. Hartmann, S. Mantl, D. Grützmacher and D. Buca, *ACS Photonics*, 2015, **2**, 1539–1545.
- 52 F. Pezzoli, A. Giorgioni, D. Patchett and M. Myronov, *ACS Photonics*, 2016, **3**, 2004–2009.
- 53 D. Saladukha, J. Doherty, S. Biswas, T. J. Ochalski and J. D. Holmes, 2017, 101081C.
- 54 M. Y. Ryu, T. R. Harris, Y. K. Yeo, R. T. Beeler and J. Kouvetakis, *Appl. Phys. Lett.*, 2013, **102**, 1–5.
- 55 D. Stange, S. Wirths, N. von den Driesch, G. Mussler, T. Stoica, Z. Ikonc, J. M. Hartmann, S. Mantl, D. Grützmacher and D. Buca, *ACS Photonics*, 2015, **2**, 1539–1545.
- 56 M. Leroux, N. Grandjean, B. Beaumont, G. Nataf, F. Semond, J. Massies, P. Gibart, M. Leroux, N. Grandjean, B. Beaumont, G. Nataf, F. Semond, J. Massies and P. Gibart, , DOI:10.1063/1.371242.
- 57 S. Al-Kabi, S. A. Ghetmiri, J. Margetis, W. Du, A. Mosleh, M. Alher, W. Dou, J. M. Grant, G. Sun, R. A. Soref, J. Tolle, B. Li, M. Mortazavi, H. A. Naseem and S. Q. Yu, *J. Electron. Mater.*, 2016, **45**, 2133–2141.
- 58 T. H. Cheng, C. Y. Ko, C. Y. Chen, K. L. Peng, G. L. Luo, C. W. Liu and H. H. Tseng, *Appl. Phys. Lett.*, 2010, **96**, 1–4.
- 59 G. Grzybowski, R. Roucka, J. Mathews, L. Jiang, R. T. Beeler, J. Kouvetakis and J. Menéndez, *Phys. Rev. B*, 2011, **84**, 205307.
- 60 S. Manna, A. Katiyar, R. Aluguri and S. K. Ray, *J. Phys. D. Appl. Phys.*, 2015, **48**, 215103.
- 61 H. Taleb and K. Abedi, *Front. Optoelectron.*, 2012, **5**, 445–456.
- 62 E. F. Schubert, E. O. Göbel, Y. Horikoshi, K. Ploog and H. J. Queisser, *Phys. Rev. B*, 1984, **30**, 813–820.
- 63 C. Pashartis and O. Rubel, *Phys. Rev. Appl.*, 2017, **7**, 1–12.

- 64 M. M. Nakata, T. M. Mazzo, G. P. Casali, F. A. La Porta and E. Longo, *Chem. Phys. Lett.*, 2015, **622**, 9–14.
- 65 K. L. Teo, J. S. Colton, P. Y. Yu, E. R. Weber and M. F. Li, 1998, **1697**, 10–13.
- 66 G. E. Yu, *Acta Mater.*, 1997, **45**, 2297–2305.
- 67 J. A. Aguiar, B. W. Reed, Q. M. Ramasse, R. Erni and N. D. Browning, *Ultramicroscopy*, 2013, **124**, 130–138.
- 68 B. . Reed and M. Sarikaya, *Ultramicroscopy*, 2002, **93**, 25–37.
- 69 B. Rafferty and L. Brown, *Phys. Rev. B*, 1998, **58**, 10326–10337.
- 70 D. Keller, S. Buecheler, P. Reinhard, F. Pianezzi, D. Pohl, A. Surrey, B. Rellinghaus, R. Erni and A. N. Tiwari, *Microsc. Microanal.*, 2014, **20**, 1246–1253.